A Simplified Model for Investigating the Magnetic Field Morphology of a Massive Clump in an Infrared Dark Cloud

Abdolreza Sharifi[1] · Mohsen Nejad-Asghar[*2]

[1] Department of Theoretical Physics, Faculty of Science, University of Mazandaran, Babolsar, Iran;
    email: ar.sharifi@stu.umz.ac.ir

[2] Department of Theoretical Physics, Faculty of Science, University of Mazandaran, Babolsar, Iran;
    *email: nejadasghar@umz.ac.ir

Abstract. Observational results of the infrared dark clouds (IRDCs) reveal that these clouds exhibit a clumpy structure with directional line-of-sight velocity gradients. Recent research by Vahadanian & Nejad-Asghar (2022, hereafter VN22) focused on the observational results of IRDC G34.43+00.24 (G34). The study concluded that G34 behaves like a rolling cylinder within the plane of the Galaxy, exhibiting a slow angular velocity of approximately $\Omega \sim 5.7 \times 10^{-14}\,\mathrm{s}^{-1}$. Using a simplified approximation for the mismatch of opposite charges, denoted by the parameter ζ, researchers demonstrated that the rotation-induced electric current can generate magnetic fields with strengths on the order of thousands of micro-Gauss in certain regions of G34. This study specifically examines the clumps within the IRDCs and employs a simplified model that incorporates a density-dependent function for the parameter ζ. Our research focuses on analyzing the magnetic field morphology within a clump while taking into account the rotation of the IRDC. To address this investigation, we examine three specific clumps - MM1, MM2, and MM3 - within G34. The findings reveal that the magnetic field strength is higher near the axis of rotation compared to distant regions from the axis. Additionally, increasing values of the angular velocity Ω and the mismatch of opposite charges ζ lead to stronger magnetic field strengths. On the other hand, the results indicate that the strength of the magnetic field is not significantly influenced by the angle between the rotational axis of the IRDC and the boundary magnetic field. These findings offer valuable insights for researchers studying the distribution of star-forming cores within clumps.

Keywords: ISM: Structure, ISM: clouds, ISM: Magnetic fields, Stars: Formation, Infrared dark clouds

1   Introduction

With the introduction of advanced mid-IR detectors in the 1990s, space facilities enabled the capture of images of the Galactic plane. These images revealed numerous dark features [1,2]. It was immediately proposed that these dark regions were dense molecular clouds ($n_{H_2} > 10^5\,\mathrm{cm}^{-3}$) with low temperatures ($T < 20\,\mathrm{K}$) that absorbed background radiation from the Galaxy's disk [3]. Subsequent research involving continuum and molecular line observations allowed for a more precise determination of the physical and chemical characteristics of these infrared dark clouds (IRDCs) [4–6]. In recent years, the availability of new observational data has provided valuable insights into the essential physical characteristics and chemical

composition of various IRDCs [7–10]. It is widely acknowledged that the cold and dense regions (referred to as clumps) within IRDCs play a significant role in the formation of clusters containing massive stars (refer to [11] for a comprehensive review). Consequently, studying the physical properties of these clumps presents an opportunity to enhance our understanding of the formation and evolution of star-forming cores within IRDCs.

Magnetic fields have a profound impact on the formation and evolution of clumpy molecular clouds [12,21]. In the case of IRDCs, which are magnetized molecular clouds [14–18], magnetic fields play a significant role in the evolution of IRDC clumps and the formation of stellar clusters [19]. Observational studies, including those mentioned above, indicate that the magnetic field strengths within IRDCs are typically several hundred micro-Gauss and can increase to thousands of micro-Gauss within clump regions. However, due to limited observational information, the detailed morphology of magnetic fields within IRDC clumps remains largely unknown. Therefore, theoretical studies can provide insights into the magnetic field structure within these clumps.

One possible explanation for the strong magnetic fields observed in IRDCs and their clumps is that they originated from the contraction of a primary atomic cloud. During this contraction, assuming the magnetic field lines are "frozen" in the gas (referred to as flux freezing), the Galactic magnetic field lines become accumulated within the cloud (e.g., [20,21]). Mestel's work demonstrated that if the initial cloud has a density of n_i and contracts to a final density of n_f, the strength of the magnetic field increases from B_i to approximately $B_f \approx B_i (n_f/n_i)^{2/3}$ ([22]). As an estimation, we assume that the initial atomic cloud has a number density of $n_i \approx 10\,\mathrm{cm}^{-3}$ and reaches the inter-clump medium within an IRDC with a density of $n_f \approx 10^3\,\mathrm{cm}^{-3}$. As a result of this process, the Galactic magnetic field increases from approximately $B_i \approx 3\,\mu\mathrm{G}$ [23] to about $B_f \approx 60\,\mu\mathrm{G}$. If we continue the same contraction process, assuming flux freezing within a clump with a density $n_f \approx 10^5\,\mathrm{cm}^{-3}$, the magnetic field inside this IRDC clump would reach the order of $B_f \approx 10^3\,\mu\mathrm{G}$. It is important to note that the assumption of flux freezing is a significant simplification and does not fully align with reality, as molecular clouds can lose their magnetic fields through the ambipolar diffusion process during their evolution [24]. However, despite this limitation, this idea provides a reasonable explanation for the observed strengths of the magnetic fields in molecular clouds and IRDCs.

In addition to the first idea, another approach suggested by [25] focuses on the generation of magnetic fields through the dynamics of IRDCs. The researchers specifically examined an IRDC named G34.43+00.24 (G34) and calculated its rotational angular velocity based on observational data. By considering the charge imbalance, they determined the electric current generated by the rotation and derived the corresponding magnetic field. Their findings demonstrated that the strength of the magnetic field resulting from the rotational dynamics of G34 is comparable to the field strengths predicted by the first idea (i.e., condensation with flux freezing). Consequently, these results highlight the importance of incorporating this mechanism into theoretical calculations.

The consideration of the charge imbalance coefficient, ζ, was a significant aspect of VN22's work. This coefficient represents a departure from the ideal assumption of equal impacts between positive and negative charges at every point within the cloud, reflecting a more realistic scenario. In their study, VN22 made the simplifying assumption that ζ remains constant throughout the G34 region. However, accurately calculating ζ in different regions of a cloud requires comprehensive observational data on the particle types, ionization fraction, and relative velocities, which we hope to achieve through advancements in telescope capabilities in the future. Currently, numerical codes such as NICIL [26,27] can be utilized to provide some estimations of ζ by simulating the movement of ions and electrons within a non-ideal magnetohydrodynamical cloud. But, this subject is out of the scope of this paper.

Here, we use some physical points of view to consider a power-law relation for the density dependence of ζ.

Our focus here is on the analysis of clumps within the IRDCs, particularly investigating the morphology of local magnetic fields within the MM1, MM2, and MM3 clumps in G34. To achieve this objective, Section 2 of this paper focuses on analyzing the gravitational equilibrium and stability of a massive clump, extracting the relevant values for radii and masses specific to the MM1, MM2, and MM3 clumps in G34. In Section 3, we calculate the current densities, while Section 4 is dedicated to determining the morphology of the magnetic fields resulting from these current densities. Finally, Section 5 provides a summary and conclusion of our findings.

2 Massive clump equilibrium and stability

We are considering a simplified model of a spherically symmetric clump within an IRDC, characterized by a radius R and in a stationary, quasi-static state ($\partial/\partial t = 0$). We assume that the cloud is in a regime dominated by thermal pressure, where equilibrium is maintained through the balance between self-gravity and thermal pressure forces. By neglecting any internal temperature gradients and assuming an isothermal equation of state ($p = a_T^2 \rho$), with $a_T = \sqrt{k_B T/\bar{m}}$ being the isothermal sound speed of the gas at temperature T and mean molecular mass $\bar{m} \approx 2.3 m_H$, we can derive the hydrostatic equilibrium equation

$$\frac{1}{\rho}\nabla p - \nabla \phi_g = 0, \tag{1}$$

where ϕ_g represents the gravitational potential, and the Poisson equation: $\nabla^2 \phi_g = 4\pi G\rho$. These equations lead to the density profile $\rho(r) = \rho_c \exp(-\psi)$, where ρ_c is the central density of the clump and $\psi \equiv \phi_g/a_T^2$. Consequently, the Poisson equation gives rise to the isothermal Lane-Emden equation

$$\frac{1}{\xi^2}\frac{d}{d\xi}\left(\xi^2 \frac{d\psi}{d\xi}\right) = \exp(-\psi), \tag{2}$$

where $\xi \equiv (4\pi G\rho_c/a_T^2)^2 r$ is the nondimensional radius. The given differential equation can be numerically integrated starting from $\xi = 0$, using the boundary conditions $\psi(0) = \psi'(0) = 0$. By solving the equation, we can obtain the ratio $\rho(\xi)/\rho_c$ (as illustrated in Figure 9.1 of [28]). The mass of this spherically symmetric cloud with nondimensional radius ξ_0 is

$$M = 0.1\xi_0^2 \left(\frac{d\psi}{d\xi}\right)_{\xi_0} \left(\frac{n_c}{10^5 \,\text{cm}^{-3}}\right)^{-1/2} \left(\frac{T}{10\,\text{K}}\right)^{3/2} \text{M}_\odot, \tag{3}$$

where $n_c \equiv \rho_c/\bar{m}$ is the number density in clump center (e.g., [29]). Therefore, if we ignore internal temperature gradients and assume an isothermal equation of state ($p = a_T^2 \rho$), only low-mass cores will exist.

However, to account for the presence of massive clumps within IRDCs, additional sources of support need to be considered [30]. One such mechanism is the magnetic fields, which can counteract gravitational forces and allow for the formation of larger clumps [31]. Another plausible supporting mechanism is turbulence, although it is currently unclear what external energy source may prevent the decay of turbulent eddies [32]. In this context, we consider internal temperature gradients as a source of support. [33] demonstrated that magnetic fluctuations within molecular clouds can generate ambipolar diffusion heating, resulting in temperature gradients within the cloud in thermal equilibrium. To quantify the magnetic
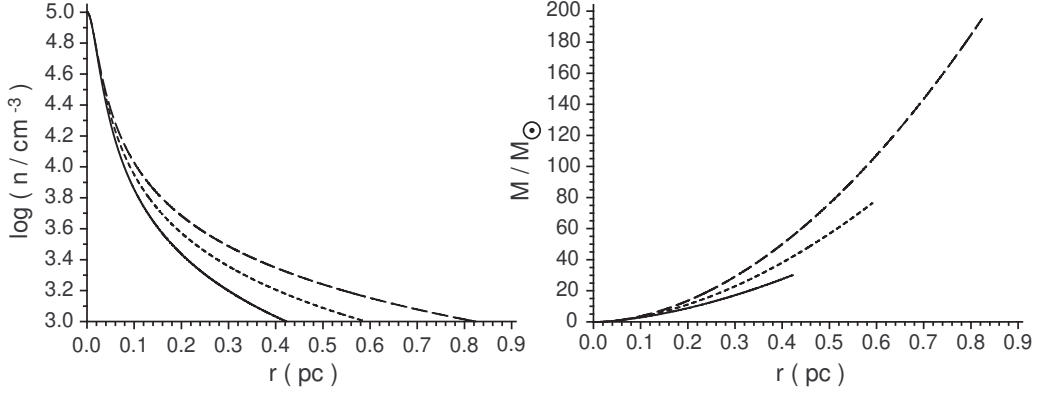
Figure 1: The number density and enclosed mass of a stationary quasi-static thermally equilibrium clump for $\tilde{\kappa} = 5$ (solid), 10 (dot), and 15 (dash). The external density of the clump is assumed to be $10^3 \, \mathrm{cm}^{-3}$.

fluctuations, the nondimensional parameter $\tilde{\kappa}$ was introduced. The findings indicated that an increase in $\tilde{\kappa}$ leads to larger radii and masses for the non-isothermal modified Bonnor-Ebert spheres. In our analysis, we assume the clump is in thermal equilibrium and refer to Figure 1 of [33] for an approximate parametric relation

$$\log(T/\mathrm{K}) = (2.55 + 0.15\tilde{\kappa}) - (0.35 + 0.03\tilde{\kappa}) \log(n/\mathrm{cm}^{-3}), \qquad (4)$$

for number densities, n, between 10^3 and $10^5 \, \mathrm{cm}^{-3}$. Also, we assume $\tilde{\kappa} \geq 5$, which indicates that the cloud is in the thermal pressure dominated regime.

Knowing the relation between temperature and density, (4), the ideal equation of state, $p = k_B n T$, leads us to determine the gradient of pressure as

$$\frac{dp}{dr} = k_B \left(T + n\frac{dT}{dn} \right) \frac{dn}{dr}. \qquad (5)$$

In this way, the hydrostatic equilibrium equation (1) becomes

$$\frac{dn}{dr} = -\frac{G\bar{m}}{k_B} \frac{M(r)n}{r^2 \left(T + n\frac{dT}{dn} \right)}, \qquad (6)$$

where $M(r)$ is the enclosed mass between $r = 0$ and radius r. In addition, the mass conservation implies that we have

$$\frac{dM}{dr} = 4\pi \bar{m} r^2 n. \qquad (7)$$

The differential equations (6) and (7) can be numerically integrated using methods such as the Runge-Kutta method. The integration starts from the origin at $r = 0$, with the boundary conditions $n(0) = n_c$ and $M(0) = 0$. Figure 1 illustrates the density and enclosed mass results for a stationary quasi-static thermally equilibrium clump with $n_c = 10^5 \, \mathrm{cm}^{-3}$.

Next, let's examine the stability of these massive equilibrium clumps. To do so, we analyze a series of pressure-bounded clumps within the IRDC. We plot their masses against the density contrast from the center to the edge, n_c/n_0, similar to Figure 9.2 of [28]. The
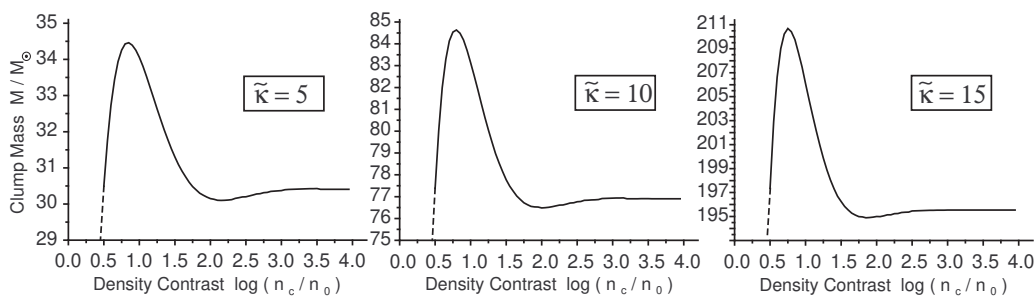
Figure 2: Sequence of non-dimensional masses of pressure-bounded clumps within an IRDC with a medium number density of $n_0 = 10^3 \, \text{cm}^{-3}$. The central density, n_c, varies from 10^3 to $10^7 \, \text{cm}^{-3}$. The mass is depicted as a function of the density contrast from the center to the edge, n_c/n_0, for values of approximately $\tilde{\kappa} = 5$, 10, and 15. Gravitationally stable regions are indicated by positive slopes on the curves, while segments with negative slopes represent unstable regions.

corresponding plot is presented in Figure 2. Initially, at the starting point of the sequence where $n_c/n_0 = 1$ and $r = 0$, the clump mass $M = 0$ is equal to zero. As the density contrast increases, the mass of the clump also increases until it reaches a maximum value. Subsequently, the mass drops to a minimum value before entering an oscillatory pattern and approaching an asymptotic limit. Whenever we encounter a maximum or minimum point on the mass curve, it indicates a stability transition for some normal mode. Specifically, clumps located to the left (right) of each maximum (minimum) point on the curve are gravitationally stable. Conversely, clumps positioned to the right (left) of these points will be gravitationally unstable. To clarify, the curve can be divided into two regions based on the slope: segments with a positive slope indicate gravitational stability, while segments with a negative slope indicate instability. Consequently, only a specific subset of the entire model sequence exhibits gravitational stability. In this context, we examine three examples of gravitationally stable clumps. These clumps have a density contrast from the center to the edge ranging from $10^5 \, \text{cm}^{-3}$ to $10^3 \, \text{cm}^{-3}$, and their respective radii are approximately $R_1 \approx 0.59$ pc, $R_2 \approx 0.82$ pc and $R_3 \approx 0.42$ pc, with masses $M_1 \approx 77 \, \text{M}_\odot$, $M_2 \approx 195 \, \text{M}_\odot$ and $M_3 \approx 30 \, \text{M}_\odot$, respectively. These clumps are approximate models of three clumps MM1, MM2 and MM3 in G34, respectively ([7]), and are suitable for probing successfully in the next sections.

3 Current density

This section focuses on investigating the influence of moving charged particles on the generation of a magnetic field within a large, stable, and rotating clump located in an IRDC. Specifically, we examine an IRDC similar to G34, which is situated near the Galactic plane. Observational data analyzed by VN22 revealed that the rotational axis of G34 closely aligns with the Galactic plane. To visualize the translational rotation of a stable equilibrium clump around the rotational axis of a G34-like IRDC, a schematic illustration is presented in Figure 3.

The motion of charged particles can generate a current density denoted as $\mathbf{J} = \sum_i n_i q_i \mathbf{v}_i - n_e e \mathbf{v}_e$, where n_i represents the number density of each species of ions with charge q_i and
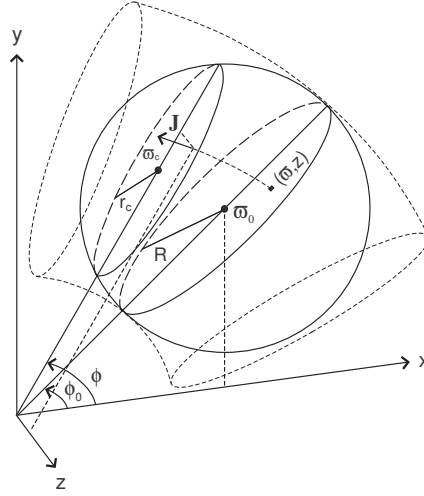
Figure 3: A schematic illustration depicting the rotational movement of an IRDC clump around an axis. The spherical cloud, characterized by a radius R, is considered to be part of a toroid shape and rotates counterclockwise around the z-axis. The center of the clump is located in the $x - y$ plane at position (ϖ_0, ϕ_0). The intersection of the clump with the ϕ-plane forms a circle with a radius of r_c and a central distance of ϖ_c. At any position (ϖ, z) in the ϕ-plane, a toroidal current density $\mathbf{J} = J_\phi \hat{e}_\phi$ is generated, which corresponds to its value in the ϕ_0-plane.

velocity $\mathbf{v}_i$, and n_e represents the number density of free electrons with charge e and velocity $\mathbf{v}_e$. The contribution of grains to the current density is negligible due to their extremely low number density. In an ideal magnetohydrodynamics scenario with complete charge neutrality, we would have $n_e \approx \sum_i n_i(q_i/e)$. However, simulations of real-world conditions indicate that molecular clouds do not conform to the assumptions of ideal magnetohydrodynamic fluids [26,27]. Recently, VN22 employed this concept to derive a straightforward parametric relationship for the current density. They made the assumption that the ions are tightly coupled with the neutral matter within the cloud, while the free electrons possess greater mobility in both forward and backward directions. In a similar vein, we assume that the ions, characterized by an average number density $\bar{n}_i$, are well-coupled to the neutral matter of the cloud and move with a velocity $\mathbf{v} = \varpi\Omega\hat{e}_\phi$. Here, Ω denotes the angular velocity of the clump's translational rotation around the rotational axis of the IRDC. Using this approach, the toroidal component of the current density, denoted as $\mathbf{J} = J_\phi \hat{e}_\phi$, can be approximated by a straightforward parametric relation: $J_\phi \approx \zeta e \bar{n}_i \varpi \Omega$. Here, ζ represents a nondimensional value that can be positive or negative, depending on the extent of charge neutrality incompleteness and the relative velocity between ions and electrons at each point within the cloud.

In their study, VN22 adopted a constant value for the parameter ζ as a simplifying assumption (specifically, $\zeta \approx 10^{-4}$) to facilitate their research process. Simulating multi-fluid systems that incorporate neutrals, electrons, and different ions can offer valuable insights into accurately calculating the degree of charge neutrality incompleteness and the relative velocities of ions and electrons at various points within the cloud. This topic is beyond the scope of this article. In this context, we adopt a physical perspective and explore

an appropriate model for ζ. We consider the notion that as molecular clouds increase in density, charged particles tend to approach each other more closely, resulting in an increase in their coupling. Conversely, the ionization fraction decreases in densely populated regions of molecular clouds due to enhanced shielding against ionizing factors. Based on this physical framework, it can be inferred that ζ decreases as the density of the cloud increases. To represent the deviation from charge neutrality and the relative speed of ions and electrons at each point within the clump ($r \leq R$), we employ a power-law function: $\zeta = \zeta_c (n/n_c)^{-\eta}$. Here, $n_c = 10^5\,\mathrm{cm}^{-3}$, $\zeta_c \approx 10^{-4}$, and $\eta > 0$ are constants.

The average number density of ions in different locations within the clump, $\bar{n}_i$, is related to the local neutral number density n. However, establishing the precise relationship between $\bar{n}_i$ and n is complex, as it involves ionization through various mechanisms and the recombination of electrons and ions on charged grains, both in the gas phase and on surfaces [34]. In the steady-state approximation within molecular clouds, we find that $\bar{n}_i \approx 3.2 \times 10^{-5} n^{1/2}$, where number densities are measured in cm^{-3} (e.g., [35], p. 362). However, it is important to note that using this steady-state approximation to equate recombination and ionization rates in dense regions of molecular clouds is a simplified approach. Nowadays, the ionization fraction in molecular clouds can be determined using numerical codes such as NICIL ([26,27]). In this study, we utilize the extracted relationship $\bar{n}_i \approx C(n/n_c)^{0.4}$, with $C \approx 6.3 \times 10^{-4}\,\mathrm{cm}^{-3}$ [36].

To complete the model, we assume a constant density in the inter-clump medium to maintain a constant value for ζ. The findings of VN22 suggest that the current density is higher in the dense central region of a clump and gradually decreases to zero towards the less dense periphery. Therefore, it is necessary to have $\eta < 0.4$. For the inter-clump medium ($R < r < R_b$), we can employ a monotonically decreasing function for the current density, denoted as $J_\phi(r) = J_\phi(R)(R_b - r)/(R_b - R)$, where R_b represents an approximate radius greater than the clump radius. For $r \geq R_b$, the current density asymptotically approaches zero, i.e., $J_\phi \to 0$. In this way, the toroidal component of current density is

$$
J_\phi = \begin{cases} \zeta_c C e \Omega \left(\dfrac{n(r)}{n_c} \right)^{0.4-\eta} \varpi, & r \leq R, \\[2em] \zeta_c C e \Omega \left(\dfrac{n_0}{n_c} \right)^{0.4-\eta} \dfrac{R_b - r}{R_b - R} \varpi, & R \leq r \leq R_b, \\[2em] 0, & r \geq R_b. \end{cases} \tag{8}
$$

In the coordinate system shown in Figure 3, any position (ϖ, z) in the ϕ_0-plane has a radius given by the equation

$$
r = \left(\frac{\varpi_0}{1\,\mathrm{pc}} \right) \left[\left(\frac{\varpi}{\varpi_0} - 1 \right)^2 + \left(\frac{z}{\varpi_0} \right)^2 \right]^{1/2} \mathrm{pc}. \tag{9}
$$

Here, ϖ_0 represents the distance between the clump center and the rotation axis. By selecting a representative value for the parameter Ω, we can calculate the azimuthal current density $J_\phi(\varpi, z)$ using the formula

$$
J_\phi(\varpi, z) = 9.1 \times 10^{-13} \left(\frac{\Omega}{10^{-14}\,\mathrm{s}^{-1}} \right) \left(\frac{\varpi}{1\,\mathrm{pc}} \right) \begin{cases} \left(\dfrac{n(r)}{n_c} \right)^{0.4-\eta}, & r \leq R, \\[2em] \left(\dfrac{n_0}{n_c} \right)^{0.4-\eta} \dfrac{R_b - r}{R_b - R}, & R \leq r \leq R_b. \end{cases} \tag{10}
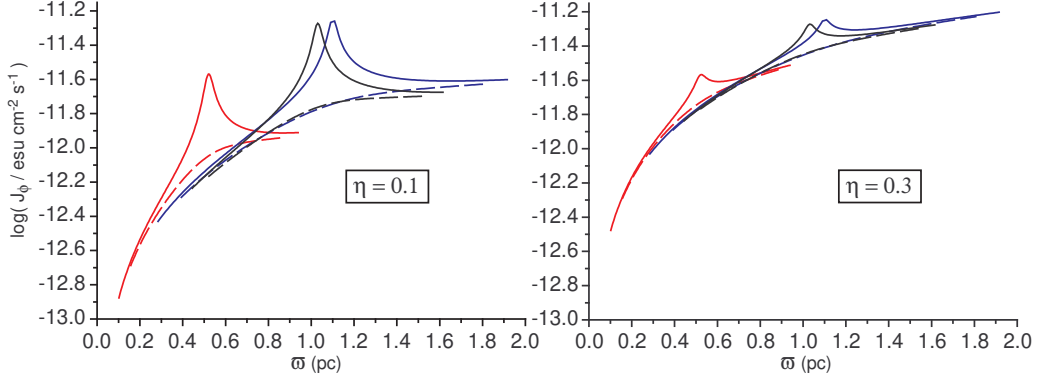$$

Figure 4: The logarithm of current density within the model clumps MM1 (black), MM2 (blue) and MM3 (red) in G34. The curves represent the current density at the central plane $z = 0$ (solid) as well as at $\pm R/2$ (dash). We consider two cases with $\eta = 0.1$ and $\eta = 0.3$. The rotational angular velocity is $\Omega = 5.7 \times 10^{-14}\,\mathrm{s}^{-1}$. The number density at the center of the clumps is $n_c = 10^5\,\mathrm{cm}^{-3}$, while it is $n_0 = 10^3\,\mathrm{cm}^{-3}$ at their periphery. In the region outside the clumps ($r > R$), we assume a linear decrease of the current density, J_ϕ, approaching zero. The sections of the curves corresponding to $R < r < R_b$ are not shown in the figures.

The current density in this equation is expressed in units of $\frac{\mathrm{esu}}{\mathrm{cm}^2\mathrm{s}}$. By solving the differential equations (6) and (7) and determining the density profile of the clump, $n(r)$, we can evaluate the current density (10) at each point (ϖ, z). In this section, we focus on three gravitationally stable clumps (MM1, MM2, and MM3) identified in the previous section, which correspond to regions within G34. The distance between each clump's center and the rotation axis, denoted as ϖ_0, is determined as follows: $1.03\,\mathrm{pc}$ for MM1, $1.10\,\mathrm{pc}$ for MM2, and $0.52\,\mathrm{pc}$ for MM3 [25]. For all models, we assume $R_b = 1.2\,R$. Figure 4 illustrates the variation of the function $J_\phi(\varpi, z)$ within these model clumps of G34, assuming $\Omega \sim 5.7 \times 10^{-14}\,\mathrm{s}^{-1}$, and considering two typical values for the free parameter η: 0.1 and 0.3.

4 Magnetic field morphology

In this section, we investigate the magnetic field morphology of a massive equilibrium stable clump in a rotating IRDC. We consider a toroidal current density model, assuming that this configuration accurately represents the system. If $J_\phi(\varpi, z)$, is applicable to all parts of the clump and its toroidal environment (as shown in Fig. 3), the magnetic field will approximately be poloidal as $\mathbf{B} = B_\varpi \hat{e}_\varpi + B_z \hat{e}_z$. In this way, Ampere's law indicates that B_ϖ and B_z are independent of the azimuthal coordinate ϕ, and also

$$\frac{\partial B_\varpi}{\partial z} - \frac{\partial B_z}{\partial \varpi} = \frac{4\pi}{c} J_\phi. \tag{11}$$

Using the absence of magnetic monopole,

$$\frac{1}{\varpi} \frac{\partial(\varpi B_\varpi)}{\partial \varpi} + \frac{\partial B_z}{\partial z} = 0, \tag{12}$$

the equation (11) leads to

$$\frac{1}{\varpi}\frac{\partial}{\partial\varpi}\left(\varpi\frac{\partial B_\varpi}{\partial\varpi}\right) + \frac{\partial^2 B_\varpi}{\partial z^2} - \frac{B_\varpi}{\varpi^2} = \frac{4\pi}{c}\frac{\partial J_\phi}{\partial z},\tag{13}$$

$$\frac{1}{\varpi}\frac{\partial}{\partial\varpi}\left(\varpi\frac{\partial B_z}{\partial\varpi}\right) + \frac{\partial^2 B_z}{\partial z^2} = -\frac{4\pi}{c}\frac{1}{\varpi}\frac{\partial}{\partial\varpi}(\varpi J_\phi),\tag{14}$$

which are the Helmholtz and Poisson equations for the components B_ϖ and B_z, respectively.

Since we are considering an axisymmetric problem, our focus is solely on the ϕ_0-plane. The results obtained for the poloidal magnetic field components B_ϖ and B_z can also be applied to other ϕ-planes. In the ϕ_0-plane, we select a square region with sides measuring $2R_b$ (approximately 2.4 times the value of R), where $-R_b \leq z \leq R_b$ and $\varpi_0 - R_b \leq \varpi \leq \varpi_0 + R_b$. We assume that the magnetic field remains constant along the perimeter of this square (as depicted in Figure 5), as $J_\phi \to 0$ approaches zero for $r > R_b$. To define the magnetic field at the boundaries of the square, we employ a constant vector field $\mathbf{B}^m$. To discretize the square region, we divide both the ϖ and z directions into M equal meshes, resulting in $M + 1$ grid points along each direction. To solve the Helmholtz and Poisson equations (13) and (14), we employ the centered finite difference formula at each interior grid point (i, j), where i and j range from 2 to M. This enables us to determine the right-hand side of the equations. Additionally, at the grid points located on the boundaries (i.e., i and j equal to 1 or $M+1$), we specify the values of the magnetic field components B_ϖ and B_z. By numerically solving equations (13) and (14), we can obtain the magnetic field components at the interior grid points. To perform this numerical solution, we utilize FISHPACK, a software package designed for solving problems involving the Helmholtz and Poisson equations [37].

Using the FISHPACK numerical solver, we can determine the values of B_ϖ and B_z at each grid point (i, j) within the mesh shown in Figure 5 by solving equations (13) and (14). To visualize the magnetic field lines, we utilize the relationship $\Delta z/B_z = \Delta\varpi/B_\varpi$ to move from the position (ϖ, z) to a new position $(\varpi + \Delta\varpi, z + \Delta z)$. To obtain the magnetic field components at each position along the magnetic field lines, interpolation is employed using the values from neighboring grid points. By applying this approach, we obtain the morphology of the magnetic field lines across all regions of the square depicted in Figure 5. In Figure 6(a), an example is presented illustrating the magnetic field lines of MM2 under the conditions $B^m = 60\,\mu G$, $\theta = 45°$, $R_B = 1.2R$ and $\eta = 0.2$. Figure 6(b) displays a color-filled contour plot representing the logarithm of magnetic field strengths in the ϕ_0-plane of MM2, measured in μG units. This visualization allows for an understanding of the distribution of magnetic field strengths within the clump. The parameters Ω, η, and θ play a crucial role in determining the magnetic field strengths inside the clumps. To examine their effects, we investigate the maximum values of magnetic field strengths within the three clumps of G34. The results of this analysis are presented in Figure 7, providing insights into the impact of these parameters on the magnetic field strengths within the clumps.

5   Summary and conclusions

In this study, we aimed to propose a novel model for the magnetic field within clumps found in IRDCs. We sought to provide a justification for the presence of magnetic fields on the order of thousands of micro-Gauss in IRDCs. The existing cloud contraction model, which assumes flux freezing, can justify the existence of these magnetic field strengths. In addition to this model, we explored a novel concept that considers the rotational dynamics of the cloud and the generation of an electric current resulting from the mismatched distribution of opposite
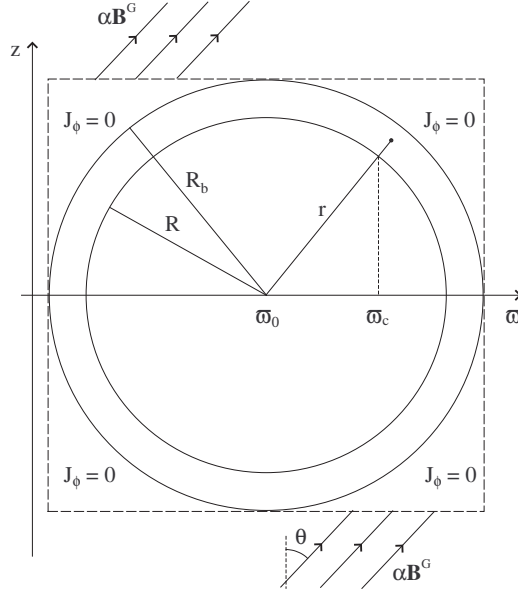
Figure 5: The square boundary of the clump in the ϕ_0-plane. The current density inside the clump $(r < R)$ and in the inter-clump medium $(R < r < R_b)$ is given by the relation (10). On the edges of the square boundary, the magnetic field is considered to be a constant vector $\mathbf{B}^m$.

charges. This current, in turn, leads to the production of a magnetic field. To quantify the extent of this charge imbalance, we introduced a coefficient called ζ. This coefficient signifies a departure from the state of equilibrium between the effects of positive and negative charges at each point within the cloud. In other words, it indicates a deviation from the ideal neutral environment typically expected in such systems. By incorporating ζ into our analysis, we aimed to better understand the mechanisms responsible for generating magnetic fields within IRDCs. In this study, we adopted a physical perspective and introduced a power relation to capture the dependence of ζ on the density of the cloud. The aim was to investigate the morphology of the magnetic field generated by the rotational dynamics of an IRDC. Our analysis focused on three specific clumps within G34, namely MM1, MM2, and MM3.

In Section 2, we examined the equilibrium and stability of these clumps. The results indicated that solely considering the pressure gradient in opposition to gravity could only account for the presence of low-mass cores. To explain the existence of high-mass clumps, we explored various mechanisms that assist the pressure gradient. Specifically, we investigated the role of temperature gradients resulting from ambipolar diffusion heating. By incorporating these factors into our analysis, we sought to understand how the interplay between pressure, gravity, and temperature gradients contributes to the formation and characteristics of clumps within IRDCs. In our approach, we incorporated a temperature-density relation described by equation (4) to investigate the variations of density and clump mass with respect to radius. These results are presented in Figure 1, providing insights into the radial profiles of these quantities within the clumps. Furthermore, we examined the stability of the clumps under different conditions. Figure 2 illustrates the stability analysis for three distinct values of the dimensionless parameter $\tilde{\kappa}$, which represents the magnetic fluctuation coefficient governing heat generation. By considering these different values, we explored the
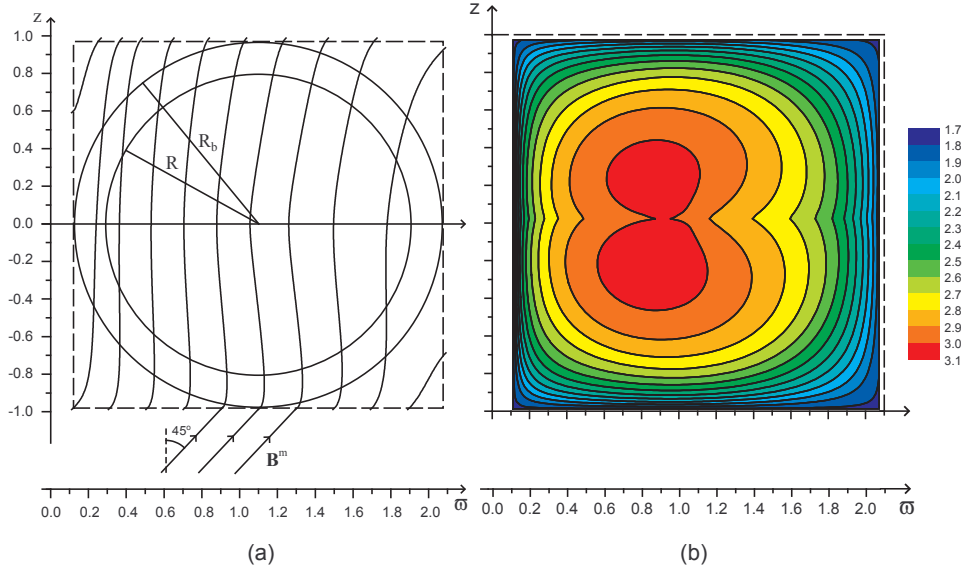
Figure 6: (a) The magnetic field lines for a representative configuration with $B^m = 60\,\mu$G, $\theta = 45°$, $R_B = 1.2R$ and $\eta = 0.2$, specifically for MM2 clump. The magnetic field lines depict the spatial distribution and directionality of the magnetic field within the clump. (b) Color-filled contour plot representing the logarithm of magnetic field strengths in the ϕ_0-plane of MM2. The magnetic field strength is measured in μG units. The scale bar provides a reference for interpreting the color-coding. Both the z-axis and the ϖ-axis are scaled in units of pc, enabling estimation of the spatial extent of the magnetic field within the clump.
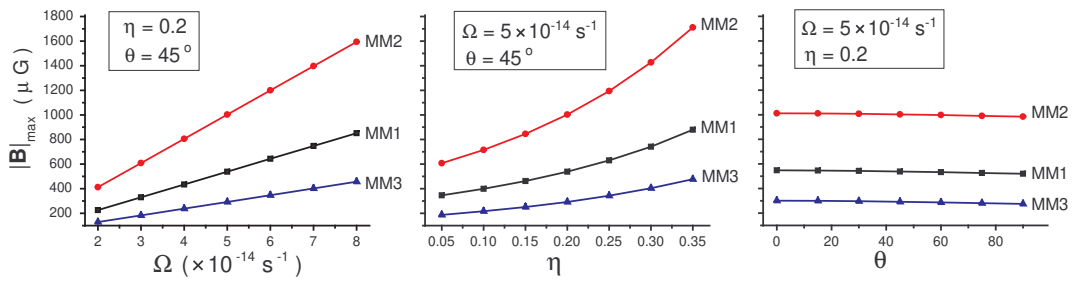

Figure 7: The maximum of magnetic field strengthes inside of three clumps of G34, according to the different values of the three parameters Ω, η and θ.

effects of magnetic fluctuations on clump stability. The results depicted in Figures 1 and 2 demonstrate that the values obtained for the mass and radius of a stable equilibrium clump align with observational findings for specific clumps. Specifically, for a value of $\tilde{\kappa} = 10$, the model matches the observations of MM1; for $\tilde{\kappa} = 15$, it corresponds to MM2; and for $\tilde{\kappa} = 5$, it is consistent with the characteristics of MM3.

To illustrate the rotation of a clump around the rotational axis of an IRDC, we provide a schematic diagram in Figure 3. Furthermore, by introducing the mismatch coefficient ζ, which accounts for deviations from the ideal state, we developed a model for the toroidal component of the current density. By including this coefficient, we aimed to capture the effects of the charge imbalance on the dynamics of the clump. In our model, we incorporated a power-law relationship between the mismatch coefficient ζ and the density. To account for factors such as ionization fraction and the decreasing current density at greater distances from the clump center, we constrained the power parameter η to values ranging from 0 and 0.4. Within regions outside the clumps, we assumed that the toroidal component of the current density decreases linearly until reaching a specified radius, R_b. Consequently, we expressed the ϕ-component of the current density inside the clumps and their surrounding areas using equation (10). Figure 4 illustrates the values of the current density for three specific clumps: MM1, MM2, and MM3.

These results demonstrate the distribution and magnitude of the current density within the clumps and their immediate surroundings based on the applied modeling approach. Once the current density is determined, we can proceed to analyze the magnetic field morphology within the clumps, including the shape of magnetic field lines and their strength. Given the toroidal component of the current density, the resulting magnetic field will exhibit a predominantly poloidal configuration. Consequently, our investigation focuses on the ϕ_0-plane, as depicted in Figure 3. This plane and its positioning relative to the boundaries with constant magnetic fields are presented in Figure 5. To solve the Helmholtz and Poisson equations (13) and (14) within the inner regions of the square in Figure 5, we utilized the FISHPACK subprogram. This numerical tool facilitated the solution of these equations, enabling us to obtain insights into the magnetic field distribution and characteristics within the clumps. The findings are presented in Figures 6 and 7, highlighting the shape and strength of the magnetic field lines within the clumps.

Three key parameters influencing these characteristics are the angular velocity of the IRDC, denoted as Ω, the power parameter η representing the mismatch of opposite charges, and the angle θ between the rotational axis of the IRDC and the boundary magnetic field. Interestingly, the results indicated that the specific values of these three parameters have a limited impact on the shape of the magnetic field lines. Consequently, we chose representative values of $\theta = 45°$, $\eta = 0.2$, and $\Omega = 5 \times 10^{-14}$ s to depict the shape of the magnetic field lines corresponding to MM2 in Figure 6(a). From this figure, it is evident that the magnetic field lines exhibit a stronger accumulation around the axis of rotation compared to regions farther away from the axis.

This observation highlights the spatial variation in the magnetic field distribution, with enhanced concentrations of magnetic field lines near the rotational axis within the MM2 clump. Figure 6(b) presents the strength of the magnetic field within the MM2 clump using a contour color-fill diagram, with the boundary magnetic field set to $60 \, \mu G$. The results demonstrate that the rotational dynamics of IRDCs can generate magnetic field strengths on the order of thousands of micro-Gauss within the clumps. These values are comparable to those resulting from cloud contraction under the assumption of flux freezing. Notably, Figure 6(b) reveals an interesting characteristic: the symmetry of the magnetic field strengths on both sides of the $z = 0$ plane. This symmetry has implications for the evolution and fragmentation of clumps as well as the formation of star-forming cores.

It suggests that the magnetic field plays a significant role in these processes, potentially influencing the dynamics and structure of the clumps as they evolve. To fully address the theoretical aspects discussed in this study, it is essential to complement the analysis with relevant observational data. With the advancement of telescopes and the upcoming launch of the James Webb Space Telescope (JWST), it is anticipated that such information will be attainable in the foreseeable future.

Of particular interest is exploring the dependence of magnetic field strengths on the three parameters: Ω, η, and θ. Our investigation focused on determining the maximum magnetic field strengths within the MM1, MM2, and MM3 clumps. The results are presented in Figure 7. As depicted in the diagrams of Figure 7, the magnetic field strength exhibits a decreasing dependence on the parameter θ, while demonstrating an increasing dependence on both Ω and η. It is worth noting that the variation in magnetic field strength due to the parameter θ within the range of 0 to 90° is less than 5%. On the other hand, the influence of the other parameters, Ω and η, on magnetic field strength is significant. Therefore, in theoretical approaches, it is crucial to consider the rotational velocity in IRDCs as well as the mismatch of opposite charges, as these factors can notably impact the strengths of magnetic fields within IRDC clumps.

References

[1] Perault, M., Omont, A., Simon, G., & et al. 1996, A&A, 315, 165.

[2] Egan, M. P., Shipman, R. F., Price, S. D., Carey, S. J., Clark, F. O., & Cohen, M. 1998, ApJ, 494, 199.

[3] Carey, S. J., Clark, F. O., Egan, M. P., Price, S. D., Shipman, R. F., & Kuchar, T. A. 1998, ApJ, 508, 721.

[4] Rathborne, J. M., Jackson, J. M., & Simon, R. 2006, ApJ, 641, 389.

[5] Ragan, E., Bergin, E. A., & Gutermuth, R. A. 2009, ApJ, 698, 324.

[6] Vasyunina, T., Linz, H., Henning, Th., Zinchenko, I., Beuther, H., & Voronkov, M. 2011, A&A, 527, 88.

[7] Tang, Y., Koch, P. M., Peretto, N., Novak, G., Duarte-Cabral, A., Chapman, N. L., Hsieh, P., & Yen, H. 2019, ApJ, 878, 10.

[8] Liu, H., Sanhueza, P., Liu, T., Zavagno, A., Tang, X., Wu, Y., & Zhang, S. 2020, ApJ, 901, 31.

[9] Fontani, F., Barnes, A. T., Caselli, P., Henshaw, J. D., Cosentino, G., Jiménez-Serra, I., Tan, J. C., Pineda, J. E., & Law, C. Y. 2021, MNRAS, 503, 4320.

[10] Miettinen, O., Mattern, M., & André, Ph. 2022, A&A, 667, 90.

[11] Zinchenko, I. 2022, arXiv221115586, to be published in Astronomical and Astrophysical Transactions, 33.

[12] Myers, P. C., & Goodman, A. A. 1988, ApJ, 326, 27.

[13] Hennebelle, P., & Inutsuka, S. 2019, FrASS, 6, 5.

[14] Santos, F. P., Busquet, G., Franco, G. A. P., Girart, J. M., & Zhang, Q. 2016, ApJ, 832, 186.

[15] Hoq, S., Clemens, D. P., Guzmán, A. E., & Cashman, L. R. 2017, ApJ, 836, 199.

[16] Juvela, M., Guillet, V., Liu, T., & et al. 2018, A&A, 620, 26.

[17] Soam, A., Liu, T., Andersson, B. G., & et al. 2019, ApJ, 883, 95.

[18] Chen, Z., Sefako, R., Yang, Y., Jiang, Z. Su, Y., Zhang, S., & Zhou, X. 2022, arXiv220703695C, submitted to MNRAS.

[19] Bahmani, N., & Nejad-Asghar, M. 2018, Ap&SS, 363, 171.

[20] Crutcher, R. M. 1999, ApJ, 520, 706.

[21] Hennebelle, P. & Inutsuka, S. 2019, FrASS, 6, 5.

[22] Mestel, L. 1966, MNRAS, 133, 265.

[23] Jansson, R., & Farrar, G. R. 2012, ApJ, 757, 14.

[24] Spitzer, L. 1978, Physical processes in the interstellar medium, A Wiley-Interscience Publication, New York: Wiley.

[25] Vahdanian, H., & Nejad-Asghar, M. 2022, MNRAS, 512, 4272.

[26] Wurster, J. 2016, PASA, 33, 41.

[27] Wurster, J. 2021, MNRAS, 501, 5873.

[28] Stahler, S. W., & Palla, F. 2004, The Formation of Stars, WILEY-VCH Verlag GmbH & Co. KGaA, Weinheim.

[29] Sanhueza, P., Garay, G., Bronfman, L., Mardones, D., May, J., & Saito, M. 2010, ApJ, 715, 18.

[30] Bertoldi, F., & McKee, C. F. 1992, ApJ, 395, 140.

[31] Mouschovias, T. C. 1976, ApJ, 206, 753.

[32] MacLow, M., Klessen, R. S., Burkert, A., & Smith, M. D. 1998, Phys. Rev. Lett., 80, 2754.

[33] Nejad-Asghar, M. 2016, Ap&SS, 361, 384.

[34] Elmegreen, B. G. 1979, ApJ, 232, 729.

[35] Shu, F. H. 1992, The Physics of Astrophysics: Gas Dynamics, University Science Books.

[36] Priestley, F. D., Wurster, J., & Viti, S. 2019, MNRAS, 488, 2357.

[37] Adams, J. C., Swarztrauber, P. N., & Sweet, R. 2016, ascl:1609.004.